

ACCEPTED VERSION

Yadong Chen, An Deng, Fan Lu, Huasheng Sun

Failure mechanism and bearing capacity of vertically loaded pile with partially-screwed shaft: experiment and simulations

Computers and Geotechnics, 2020; 118:103337-1-103337-13

© 2019 Elsevier Ltd. All rights reserved.

This manuscript version is made available under the CC-BY-NC-ND 4.0 license

<http://creativecommons.org/licenses/by-nc-nd/4.0/>

Final publication at: <http://dx.doi.org/10.1016/j.compgeo.2019.103337>

PERMISSIONS

<https://www.elsevier.com/about/policies/sharing>

Accepted Manuscript

Authors can share their [accepted manuscript](#):

24 Month Embargo

After the embargo period

- via non-commercial hosting platforms such as their institutional repository
- via commercial sites with which Elsevier has an agreement

In all cases [accepted manuscripts](#) should:

- link to the formal publication via its DOI
- bear a CC-BY-NC-ND license – this is easy to do
- if aggregated with other manuscripts, for example in a repository or other site, be shared in alignment with our [hosting policy](#)
- not be added to or enhanced in any way to appear more like, or to substitute for, the published journal article

22 March 2022

<http://hdl.handle.net/2440/123119>

1 **Failure mechanism and bearing capacity of vertically loaded pile with**
2 **partially-screwed shaft: experiment and simulations**

3
4 Yadong Chen^a, An Deng^{*b}, Fan Lu^c, and Huasheng Sun^a

5
6 ^a Faculty of Architecture and Civil Engineering

7 Huaiyin Institute of Technology

8 Huaian 223001, China

9
10 *Corresponding author

11 ^bSchool of Civil, Environmental and Mining Engineering

12 The University of Adelaide

13 Adelaide SA 5000, Australia

14 E-mail addresses: an.deng@adelaide.edu.au

15
16 ^c College of Transportation Science & Engineering

17 Nanjing TECH University

18 Nanjing 210000, China

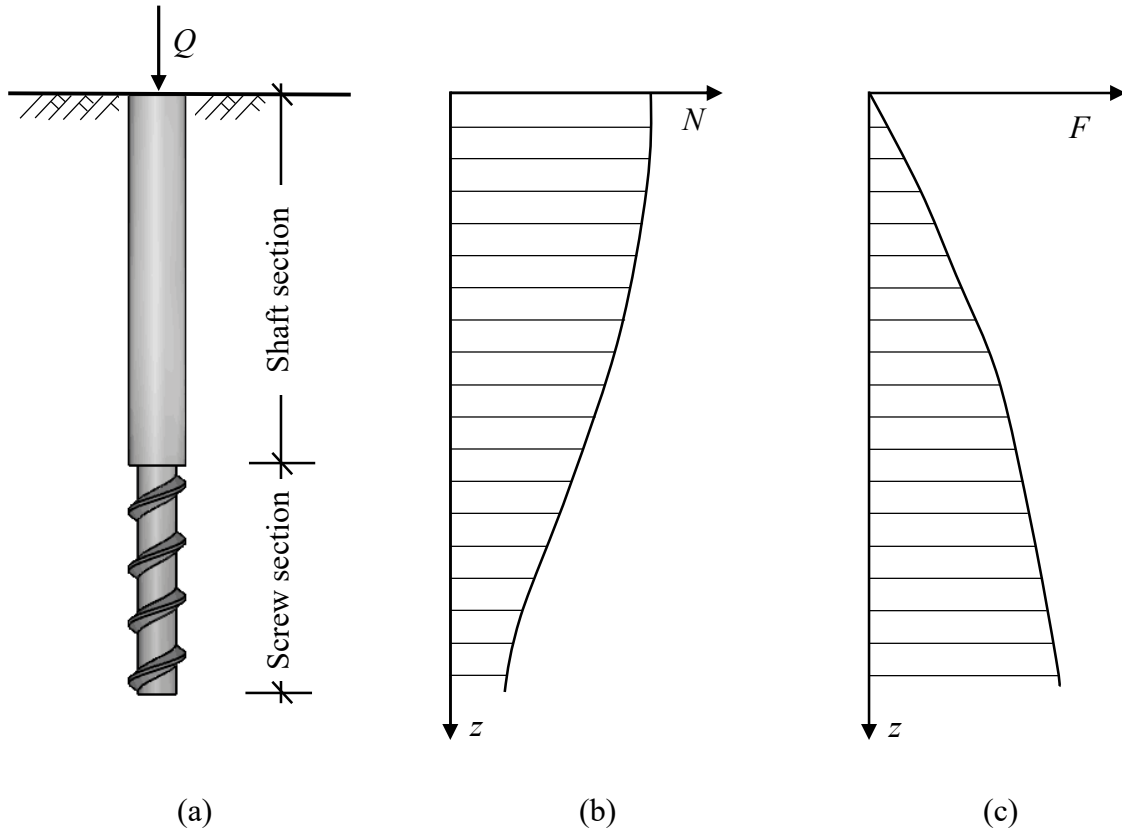
22 **Abstract:** An experimental and numerical investigation on performance of piles with
23 partially-screwed shaft that were installed in sands was presented. Static load tests were
24 conducted on a series of model piles to examine pile–sand interactions and the bearing
25 capacity. The tested piles were varied in thread pitch in order to examine its effects on pile
26 performance. Digital imaging correlations were used to visualise the failure slips of sands at
27 locations of interest. The test results were used to validate a discrete element model (DEM)
28 that was developed to assess the pile–sand interactions at micro-scale. The DEM model was
29 applied to examine the effects of important pile geometric characteristics on the load
30 transfer and bearing capacity of piles. The characteristics included the pitch, length of screw
31 section, and shaft diameter. The simulation results suggested that the screw section and
32 bottommost thread significantly influenced the pile bearing capacity. An optimum geometry
33 of pile that maximised pile–sand interactions and prompted the pile performance was
34 suggested.

35 **Keywords:** screw–shaft pile; bearing capacity; failure slip; pile–soil interaction; load
36 transfer

37

38 **1 Introduction**

39 Piles with screwed shaft, or partially-screwed piles, have been increasingly used as an
40 improved foundation solution in a variety of applications [1, 2]. The wide acceptance in
41 practice is mainly due to the piles providing advantages in the aspects of i) ease and fast
42 installation with minimal vibration or noise, and minimal spoils, and ii) enhanced bearing
43 capacity [3, 4]. Broadly, such piles can be prefabricated as a shaft with single- or
44 multiple-helix auger welded, or be cast on-site by using auger piling equipment. For the latter,
45 continuous-flight-auger (CFA) and drilled-displacement (DD) rig are the major piling
46 equipment in the market. Both equipment advances an auger into the ground to create void
47 space for pile. In advancing the auger, the surrounding soils are displaced laterally (not
48 extracted) which compacts the soils and adds to the development of pile bearing capacity. DD
49 piles use a larger diameter auger (or casing and cavity expansion element) and therefore
50 produce greater soil displacement than CFA pile does. Upon lifting up the auger, both
51 equipment fill up the created void with grout and in the meantime determine the direction of
52 auger rotation. If rotated in a counter-wise direction, a series of threads, as parts of the created
53 void at the depths of interest, are formed and filled up by the poured grout. The grouting
54 usually produces more noticeable threads (e.g. greater threads depth) for CFA piles, as
55 opposed to DD piles. For both DD and CFA piles, their lifting processes can allow the auger
56 to rotate as occurred in the course of advancing, or inhibit the auger rotation. In these
57 circumstances, the existing threads are levelled off and a smooth or nearly smooth shaft is
58 formed. A partially-screwed shaft as illustrated in Figure 1 (a) is formed.



59 Figure 1 The schematic of partially-screwed pile: (a) geometry, (b) diagram of axial force
 60 distribution, and (c) diagram of skin friction distribution.

61
 62 The partially-screwed pile expects to optimise performance of pile. The diameter of the upper
 63 shaft section is enlarged or intact which increases the resistance of this section counteracting
 64 the greater axial force at the top as presented in Figure 1 (b). Similar optimisation occurs to
 65 the screw section. The presence of the screw threads adds to the shaft skin friction which
 66 increases with depth as illustrated in Figure 1 (c), and therefore contributes to the pile–soil
 67 interactions, as well as the load-carrying capacity of the pile. The performance optimisation
 68 has been verified directly or indirectly in earlier laboratory model tests and field applications
 69 for piles installed in clayey or sandy soils. Chen *et al.* [5] conducted a laboratory-scale model

70 test on the performance of the partially-screwed pile in sands and found the ultimate bearing
71 capacity was improved by up to 43%. A significant contribution arose from the screw section,
72 in particular the bottommost thread. A similar increase of shaft skin friction was observed in
73 the static load test conducted for the screwed pile installed in silty clay as reported in Zuo *et*
74 *al.* [6]. Apart from the skin friction, a vertical support was also found of evolving from the
75 presence of the threads or helix in field applications [7-10]. Some field tests also investigated
76 important factors that contribute to pile performance. The factors include pile diameter, thread
77 depth and pitch Sakr [11], soil types Fahmy and El Naggar [12], and the pile installation
78 method Choi *et al.* [13]. These studies also suggested zoned failure modes and corresponding
79 load-bearing models. The failure patterns were mainly dependent on the proportion of screw
80 section and soil types.

81
82 Although the presence of screwed shaft has improved performance of pile, the foundation
83 design is usually conducted by referring to methods for shafts which however fail to take
84 advantage of screw threads. An important performance indicator is the ultimate bearing
85 capacity. One approach as suggested in [14] was to estimate the bearing capacity in terms of
86 load–settlement curves obtained from pile load tests. Li and Deng [15] used a hyperbolic
87 function to represent the curve and predict the ultimate bearing capacity. To determine the
88 ultimate bearing capacity, there are no agreed criteria, e.g., the 0.08D suggested in [1] and
89 0.1D in [14]. Regardless of the suggested criteria, the static loading based approach however
90 is not financially viable in some circumstances where soil profiles vary spatially and a lot of

91 load tests are required. In addition to load tests, numerical simulations were performed to
92 examine pile performance from a different perspective. The methods included the finite
93 element method e.g. Meng *et al.* [16] and Qian *et al.* [17], digital image correlation and
94 discrete element method such as Chen *et al.* [5]. The numerical simulations enable a range of
95 piling parameters to be considered, including soil conditions and pile geometry, and are able
96 to provide extensive outputs of ranging from the bearing capacity, to the force and
97 displacement at any location or time. For example, Qian *et al.* [17] used three-dimensional
98 finite element method to examine skin friction distribution and suggested that the friction
99 increases due to the interlocking between threads and surrounding soils. A further numerical
100 study by George *et al.* [18] suggested that the pile capacity is also dependent on the screw
101 configuration and its depth. Similar results were confirmed in Lee *et al.* [19] who stated that
102 the ultimate bearing capacity and skin friction of screw piles outperform those of comparable
103 shaft piles. From these studies, it is seen that the numerical work extends the scenarios to be
104 examined.

105

106 Whereas earlier research work has verified the performance of the partially-screwed piles,
107 discrepancies between the model predictions and the field test results still exist [14, 20].
108 Given this, the design of the piles is usually conducted by trials-and-errors, which
109 compromises QA/QC in practice and causes a loss on time and cost. The underrepresented
110 design is resulted partially from the unclear understanding of load transfer of pile, in
111 particular, the thread- and shaft–soil interactions. The effects of screw threads are misleading,

112 such as '*the more the better*', and as a result the pitch is arranged in a less efficient means.
113 Similarly arbitrary design occurs to the allocation of screw section versus the shaft section,
114 leading to a different range of length of the screw section where the soil conditions remain the
115 same, or vice versa. These sub-optimal design practices most likely underestimate the pile
116 performance and should be avoided.

117

118 This study was conducted to examine the performance of pile by considering the pile
119 geometry, in particular the details of the thread pitch, length of screw section and shaft
120 diameter. The goals were achieved through conducting load tests on a series of model piles.
121 The piles were varied in screw thread. The digital image correlation was used to capture the
122 pile performance at micro-scale. A numerical model was developed and applied to examine
123 thread- and shaft–soil interactions and to gain an understanding of pile failure mechanism. A
124 parametric study was conducted on representative piles to optimise its design.

125

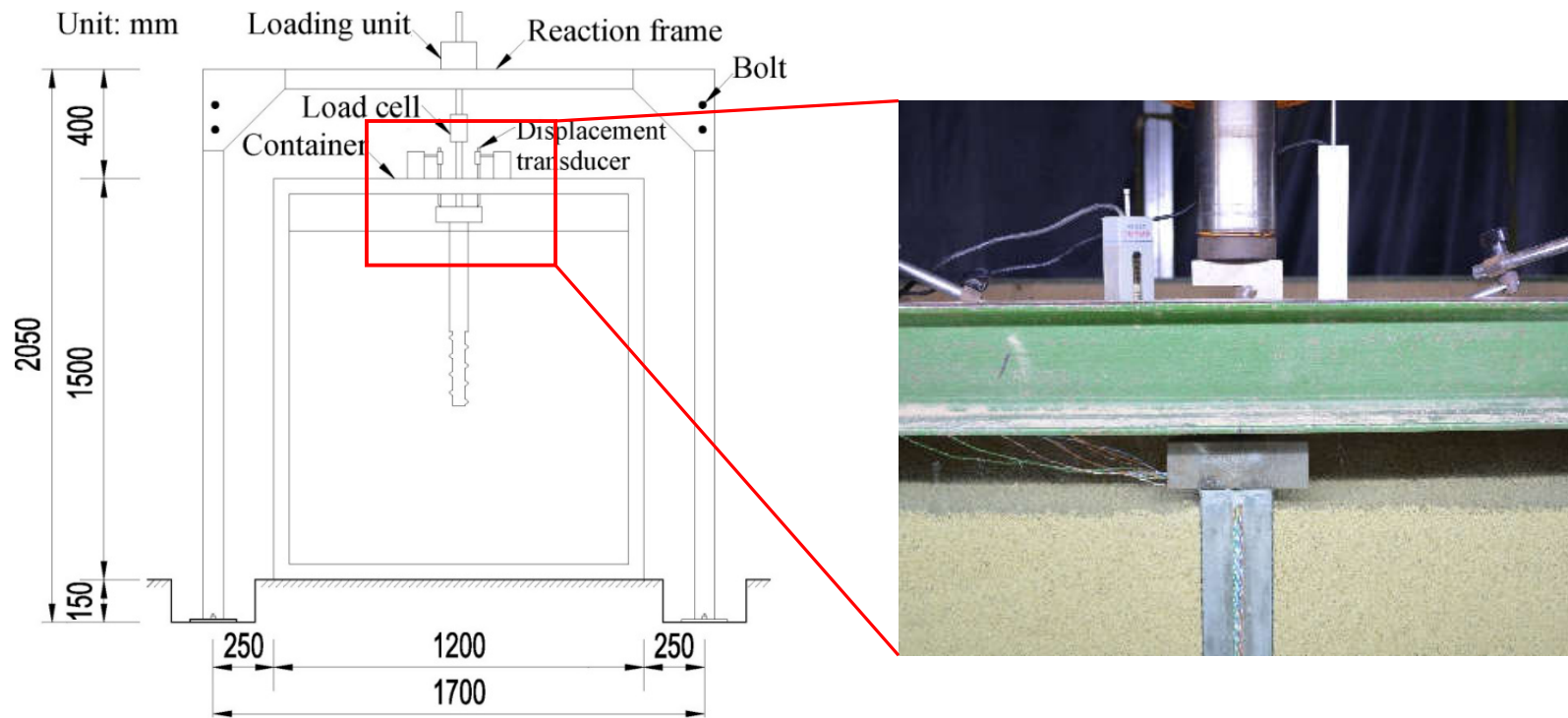
126 **2 Experimental Program**

127 **2.1 Test set-up**

128 The set-up that was used for the load test of pile is presented in Figure 2. This set-up has been
129 successfully used in the earlier study [5] to conduct pile load tests. Some important
130 information of the set-up is presented here. The set-up included a rigid cuboid container with
131 the internal space of 1,200 (L) × 1,000 (W) × 1,500 (D) mm. The front panel of the container
132 was transparent that enabled observing and imaging progress of tests. A force reaction frame

133 was constructed above the container. The reaction was applied through a hydraulic jack,
134 plunger and loading cap that were mounted above the pile head, and was recorded by a load
135 cell. Two displacement transducers were clamped to the reaction frame to measure the
136 settlement of pile head. The container was used to accommodate a volume of sand and the
137 pile to be tested. The sands were air-dried with a median diameter $D_{50} = 0.65$ mm, maximum
138 void ratio $e_{\max} = 1.01$, minimum void ratio $e_{\min} = 0.60$, density of 1.53 g/cm^3 , and the angle of
139 internal friction of 32.1° . The pile was pre-installed, which is a solution adopted in many
140 laboratory studies [21, 22]. Specifically, a semicircular pile was positioned and fastened, with
141 its cross section in contact with the front panel, enabling the imaging purpose. As discussed in
142 [5], the use of a semicircular pile is able to yield test results as obtained from the circular pile,
143 only if the pile–wall contact surface is smooth which was attained by smearing a thin layer of
144 silicone grease on the contact surface. The size and boundary effects were also marginal as
145 the pile diameter D was 20 times greater than the average sand particle size and the
146 boundaries were about $5D$ apart from the shaft. Once the pile had been erected, the sands
147 were placed into the container. The sands were placed in lifts, 100 mm each, to a height of
148 1,200 mm. Each lift was compacted uniformly using a vibro plate compactor, targeting a
149 relative density of about 68%. The compactor provides a vibratory force output of up to 200
150 kgf, at the capacity of 250 w. The compactor plate measures 270×190 mm, which provides a
151 decent coverage of compaction and thus energy consistency. The plate uses fine edge and
152 corner which offers accessibility to difficult areas including the chamber corners, shaft-screw
153 junction and the under-threads.

154



155

156

(a)

(b)

157 Figure 2 The set-up of load test for pile installed in sand: (a) diagram of the test cuboid container, and (b) load cell, displacement transducer,

158

container, sands and pile head.

159

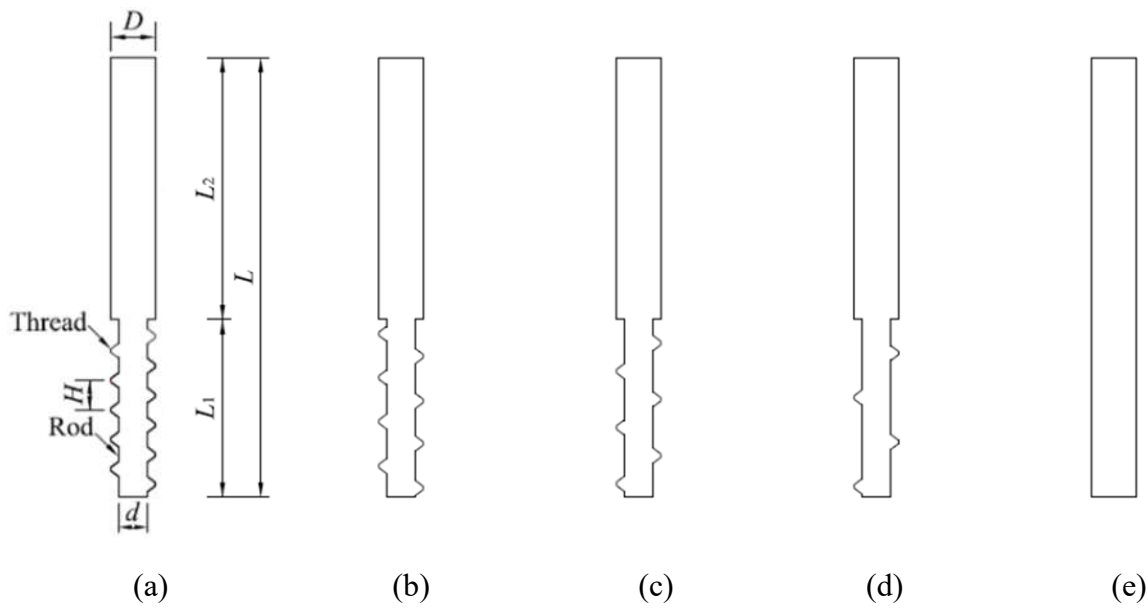
160 We designed and tested five piles as summarised in Table 1. These piles were varied in
161 thread pitches which were 0, 40, 60, 80 and 120 mm. The pitch of zero represented the
162 control pile with a smooth shaft, which was named pile $P0$ whereby the ‘0’ suggests the
163 pitch. A similar convention was used to name the other piles, i.e., $P40$, $P60$, $P80$ and $P120$.
164 For the five piles, the remainders of geometric characteristics were the same, including the
165 pile length $L = 600$ mm, shaft diameter $D = 60$ mm, rod diameter $d = 40$ mm, and the length
166 of screw section $L_1 = 240$ mm, as presented in Figure 3. The consistency in geometric
167 characteristics was expected to highlight the effects of pitch. As in [21, 23], we used a stiff
168 aluminium material to fabricate the pile. The material was stiff enough to replicate concrete
169 materials. We also replicated a rough surface by affixing a layer of sandpaper #360 on the
170 pile skin. The pile–soil interface effective friction angle, δ' , was determined by conducting
171 the direct shear tests as suggested in [24]. The aluminum block that was affixed with the
172 sandpaper was placed in the lower shear box, with its surface flush with the shear interface.
173 The upper shear box was filled with the same sands as used in the model tests. Three levels
174 of vertical loads were used: 50, 100 and 200 kPa. The pile–soil interface effective friction
175 angle was determined as 34.7° .

176 Table 1 Geometric properties of model piles that were subjected to static load tests.

Pile	Pile length L (mm)	Shaft diameter D (mm)	Rod diameter d (mm)	Length of	
				screw section L_1 (mm)	Thread pitch H (mm)
$P0$	600	60	60	0	0

<i>P40</i>	600	60	40	240	40
<i>P60</i>	600	60	40	240	60
<i>P80</i>	600	60	40	240	80
<i>P120</i>	600	60	40	240	120

177



178

179

180 Figure 3 The vertical cross sections of piles: (a) *P40*, (b) *P60*, (c) *P80*, (d) *P120*, and (e)
 181 *P0*.

182

183 We loaded the piles using a displacement-controlled method, as in a static load test. The
 184 pile was compressed downward at a rate of 0.3 mm/min, equally 0.05% strain per minute.

185 The loading continued until the pile attained a failure or settlement $S = 20$ mm (i.e. 3.3%
 186 settlement rate), whichever occurred earlier. A test lasted about 70 minutes and in the test

187 we recorded the following results: the force acted on the pile, displacement of pile head, and

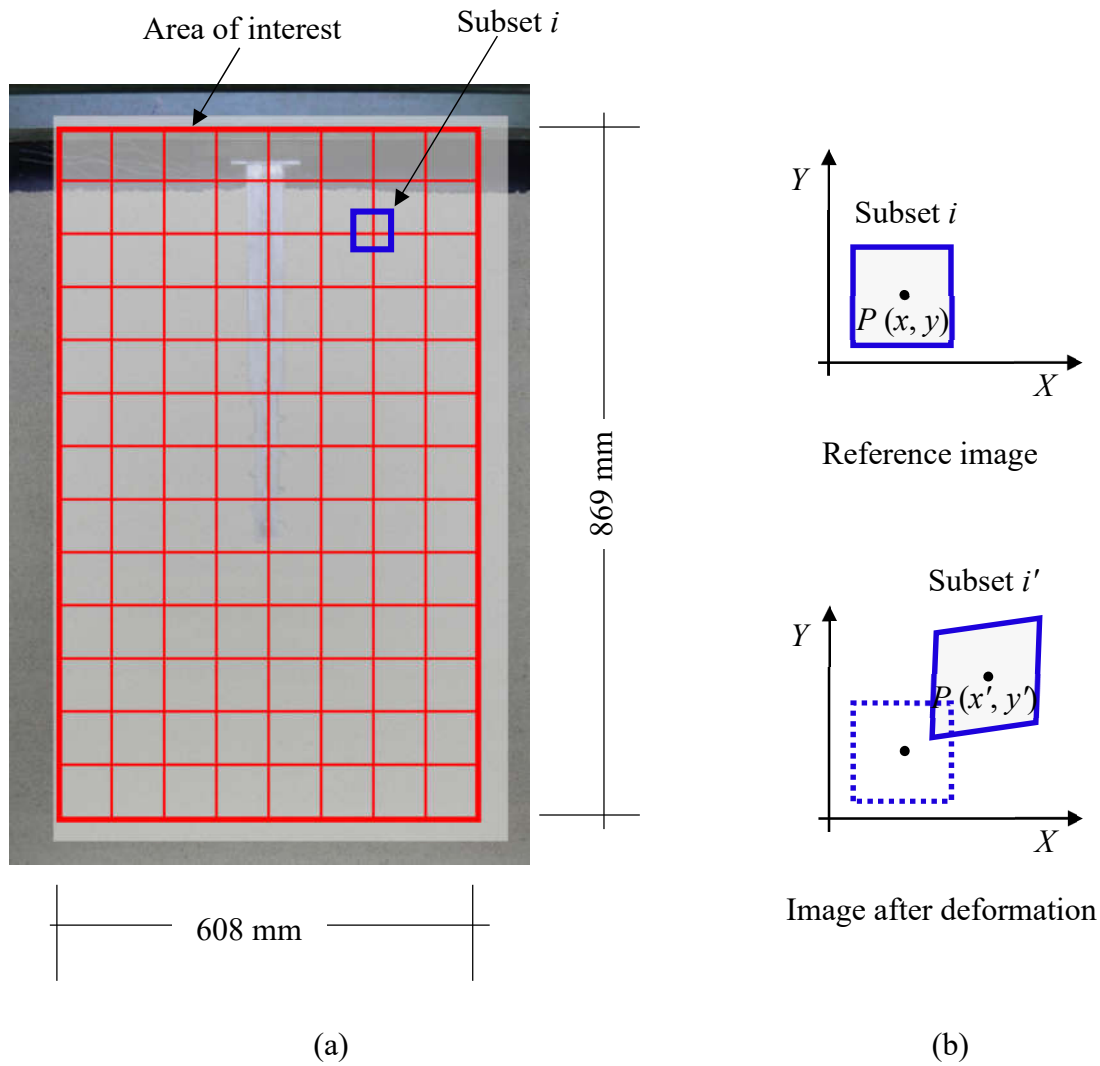
188 the displacement of sands, as a function of locations, by the digital image correlation (DIC)

189 technique.

190

191 **2.2 Digital image correlation**

192 The DIC is a tool developed to track and visualise full-field displacement and strains of
193 deformed materials. As opposed to strain gauges and extensometers, the DIC gathers fine and
194 extensive details of deformation, and maps it into displacement vectors. An area of interest
195 (AOI) is specified and divided into an evenly spaced grid as presented in Figure 4 (a). On the
196 grid, each junction corresponds to a subset that is pre-defined. On Figure 4 (b) for example,
197 subset i encompasses a unique set of pixels and grey-scale intensities which are unique, and
198 thus its centre point, $P(x, y)$, is trackable when the deformation occurs. The tracking is
199 conducted using selected correlation functions such as cross-correlation or normalised
200 cross-correlation [25-27]. The correlations compare grey-scale intensities of subset i in the
201 reference image and adjacent subsets in the image obtained after the deformation, and identify
202 target subset i and its centre point, $P(x', y')$. Full-field correlations across all of the subsets,
203 along with the progress of deformation, provide the strain- or displacement fields of interest.



204 Figure 4 Diagrams for (a) DIC set-up, and (b) the correlation concept.

205

206 In the current study, the AOI had a coverage of 869 (H) \times 608 (W) mm, equally 5,000 (H) \times
 207 3,500 (W) pixel, which covers the most area of influence. On the grid, each junction
 208 corresponded to a subset of 64 \times 64 pixel, the size of which, as per [28], provided sufficient
 209 grey-scale intensities for deformation tracking. A rate of one image per 0.4 mm pile settlement
 210 was used to attain a smooth and continuous tracking of deformation, and thus a total of 50
 211 images were obtained in one test. It is noteworthy that we performed a validation test to
 212 testify the accuracy of DIC correlation. We offset, on the canvas, a reference image of AOI by

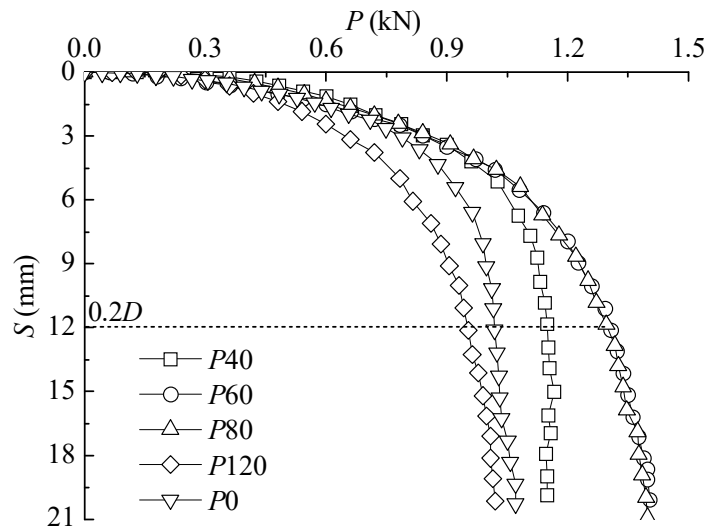
213 3 pixels. The same subset of 64×64 pixel was used to correlate the new and the reference
214 images. The obtained displacement vectors suggested a displacement of 2.938 pixels with the
215 standard deviation of 0.022 pixels. The pixel displacement agreed very well with the offset
216 value and therefore the performance of DIC correlation was verified.

217

218 **2.3 Load–settlement curves**

219 The load–settlement (P – S) curves that were obtained for the tested piles are presented in
220 Figure 5. All curves present a nonlinear relationship, as obtained for a usual shaft pile. The
221 curves can be divided into three sections: the nearly linear development at the outset of
222 from zero to approximately 0.8 mm settlement, the nonlinear yielding from 0.8 to 5.0 mm,
223 and the approximately linear drop throughout to the end of tests. Although there is similarity
224 in the curve nonlinearity, the load resistances that were gained in each test varied clearly.
225 Piles $P60$ and $P80$, which used pitch $H = 60$ and 80 mm respectively, yielded nearly the
226 same and the greatest resistance where the settlements were the same, as opposed to the
227 other piles. Pile $P40$ provided the second greatest resistance, and was followed by piles $P0$
228 and $P120$. It is noteworthy that pile $P40$ used the least pitch $H = 40$ mm (i.e. a greater
229 number of thread count), but did not provide the resistance as much as piles $P60$ and $P80$
230 did. Similar results were obtained in Tsuha *et al.* [29] who used a centrifugal method to
231 examine the contribution of pitch to pile bearing capacity. This implies there is an optimum
232 thread pitch for the pile bearing capacity, at least for the model piles tested in this study. A
233 similarly interesting comparison between piles $P120$ and $P0$ was conducted. The former
234 shaft was partially-screwed (with a pitch $H = 120$ mm), but unexpectedly failed to

235 outperform the control pile $P0$ which used a smooth shaft. The performance difference
 236 suggests that the base resistance outweighs the skin friction when examine the pile bearing
 237 capacity. In addition, it is plausible to claim a trade-off that likely arises from the presence
 238 of threads and the shaft diameter. The threads are present to contribute to the load resistance,
 239 but somehow are at the cost of reducing the shaft diameter which comprises the skin friction.
 240 The existence of the trade-off suggests the need of optimising the thread pitch against the
 241 shaft diameter.

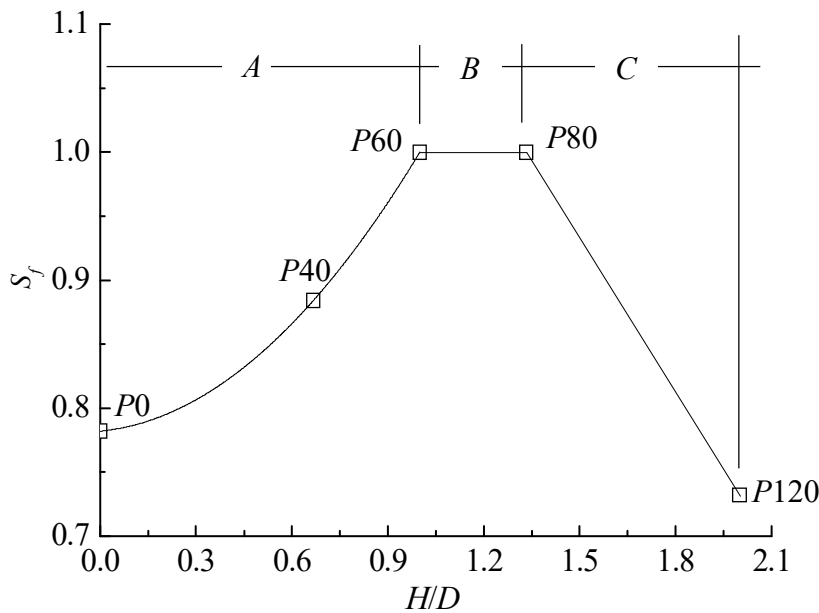


242
 243 Figure 5 The P - S curves of piles with varied thread pitches.

244
 245 We defined the dimension ratio, $\chi = H/D$, as the thread pitch to the shaft diameter. As per [10],
 246 the ratio plays an important role in influencing the pile bearing capacity. We examined the
 247 ultimate bearing capacity Q_u and as discussed in [5] used the settlement $S = 0.2D$ criterion to
 248 determine Q_u of the piles. The ultimate bearing capacity were $Q_u = 0.945$ kN for pile $P0$,
 249 1.150 kN for $P40$, 1.301 kN for $P60$, 1.301 kN for $P80$, and 0.952 kN for $P120$. We then
 250 defined S_f , the normalised ultimate bearing capacity to pile $P80$'s, and plotted S_f against the
 251 dimension ratio H/D as presented in Figure 6. The curve includes three sections: A , B and C .

252 In section *A* where H/D ranges from 0 to 1.0, S_f increases nonlinearly with H/D , suggesting
 253 the advantage of increasing the pitch up to the value of the diameter. If the pitch is equal to
 254 the value of the diameter, the curve moves into section *B*, and in this section the bearing
 255 capacity S_f reaches its crest and remains unchanged until $H/D = 1.33$. In this section, an
 256 optimisation of sands–shaft–thread interaction was obtained. If H/D increases from 1.33 to
 257 2.0 as in section *C*, S_f decreases clearly. The three sections can be expressed into Eq. (1). This
 258 equation was developed based on the number of piles tested in the laboratory and is subject to
 259 verification and improvement through additional tests. The equation however suggests the
 260 need to optimise pile performance and in some circumstances can referred to as the point of
 261 departure where to determine the ultimate bearing capacity of partially-screwed piles.

$$S_f = \begin{cases} 0.782 + 0.023\left(\frac{H}{D}\right) + 0.195\left(\frac{H}{D}\right)^2 & \text{for } 0 < \frac{H}{D} < 1.0 \\ 1.0 & \text{for } 1.0 \leq \frac{H}{D} \leq 1.33 \\ 1.532 - 0.4\left(\frac{H}{D}\right) & \text{for } 1.33 < \frac{H}{D} < 2.0 \end{cases} \quad (1)$$

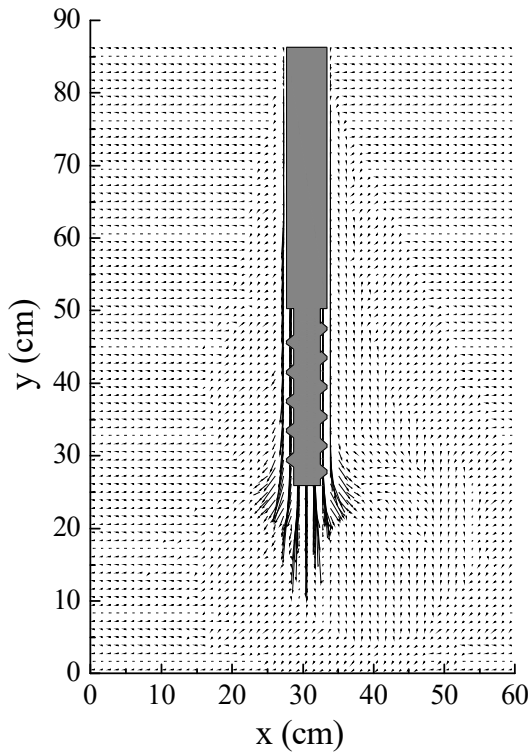


262
 263 Figure 6 The relationship between the normalised ultimate bearing capacity S_f and the
 264 dimension ratio H/D for the piles in static load tests.

265

266 **2.4 Sand displacement vectors**

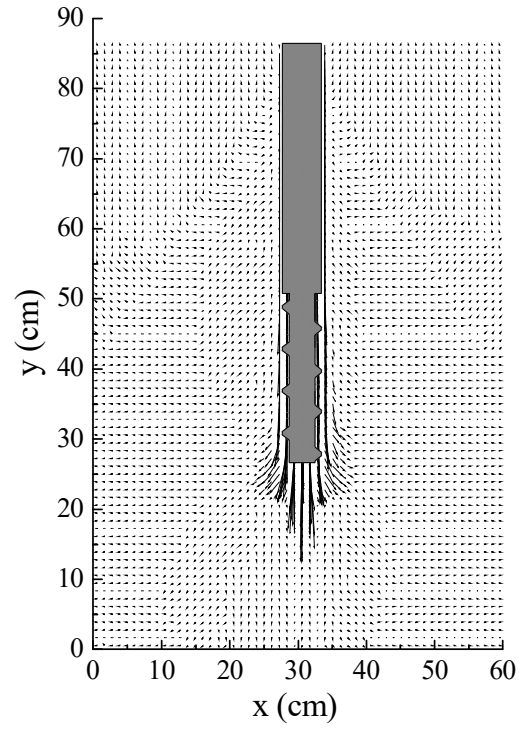
267 The maps of sand displacement vectors obtained by the DIC technique are presented in
268 Figure 7. These maps apply respectively to four piles *P40*, *P60*, *P80* and *P120* at the point
269 of settlement $S = 20$ mm. The sands that were adjacent to the piles, including the upper
270 shafts, lower screw sections, and the bases, moved downward or so at varied orientations.
271 The magnitudes of displacement, which are suggested by the vectors length, were greater at
272 locations near the base and screw section than elsewhere, and varied among the piles. For
273 piles *P40* and *P60* [Figure 7 (a–b)], which used relatively less pitches and greater thread
274 counts, a limited volume of sands around the screw sections displaced; greater volumes of
275 sand near the base were displaced or influenced. The closely-arranged threads likely
276 constrained the movement of sand particles and inhibited the spread of interlocking force to
277 the surrounding sands. With the increase of thread pitch as in piles *P80* and *P120* [Figure 7
278 (c–d)], the spaces between threads were opened up and appeared to effectively engage
279 additional sands to counteract the plunging piles, as evidenced by the globes of influence
280 that are plotted around the screw sections.



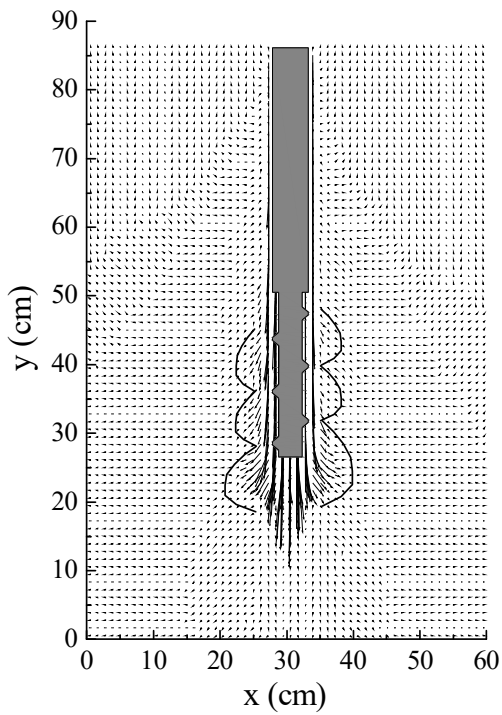
281

282

(a)



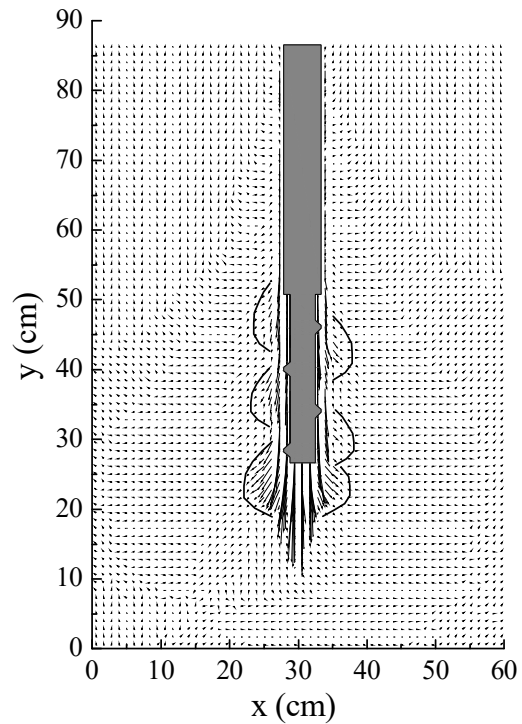
(b)



283

284

(c)



(d)

285 Figure 7 The maps of sand displacement vectors, drawn to the same scale, of the
 286 partially-screwed piles: (a) *P40*, (b) *P60*, (c) *P80*, and (d) *P120*, which were compressed to

287 settlement $S = 20$ mm under the load tests.

288

289 **2.5 Sand displacement contours**

290 To gain a further insight into the sand particle displacement, the sand displacement vectors

291 in Figure 7 were represented into displacement contours, as presented in Figure 8. These

292 contours ranged from displacement 0 to up to 18 mm and were drawn at 0.1 mm interval.

293 As its name suggests, a contour is usually a closed plot on which the points displace to the

294 same value represented by the contour. In addition, a greater area enclosed by the

295 same-value contours suggests a greater volume of sands that are influenced to counteract

296 the pile penetration, and thus a high bearing capacity. This is the case for piles $P60$ and $P80$

297 as presented in Figure 8 (b–c). For example, their 0.2 mm contours enclose relatively larger

298 areas, as opposed to the corresponding ones for piles $P40$ and $P120$. Similar results are

299 identified for the remainders of contours. The findings that are obtained from the contours

300 comparison agree with the bearing capacity results represented by the P – S curves in Figure

301 5. The displacement contours can also be used to identify the scope of influence, as opposed

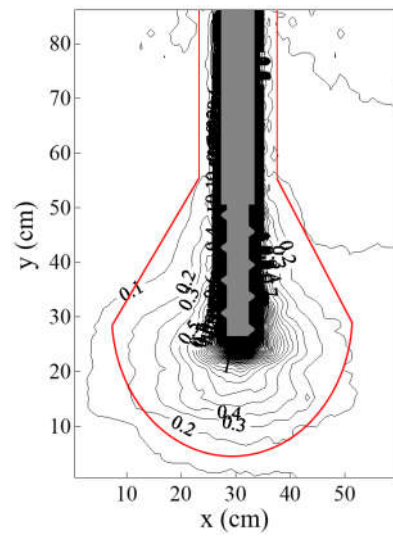
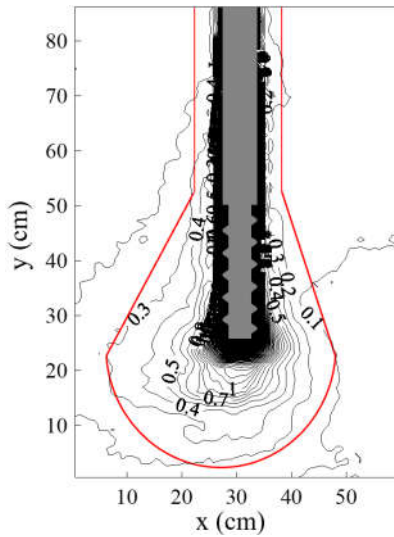
302 to nearly intact zones. The scopes were marked out as presented on the diagrams. Although

303 all scopes of influence develop into a *flask* shape, the shapes differ, mainly in the globes at

304 the bottom. The globes decrease in size in the order of piles: $P80$, $P60$, $P40$ and $P120$. For

305 pile $P80$, the failure slip of interest sits about $1D$ off the shaft, $2D$ to $4D$ off the screw

306 section or the base depending on the locations.

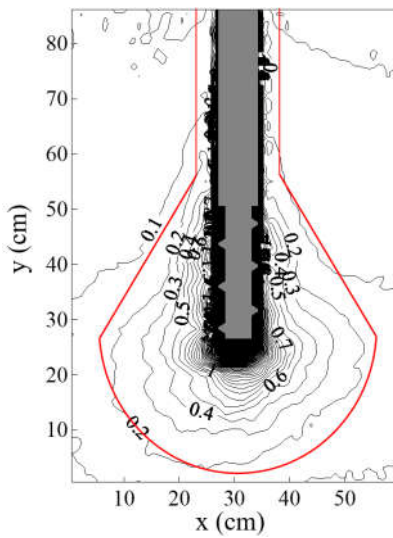


307

308

(a)

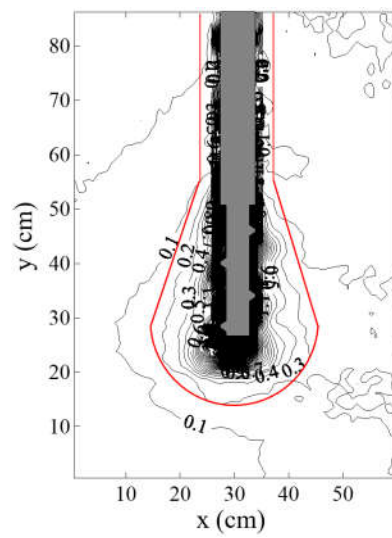
(b)



309

310

(c)



(d)

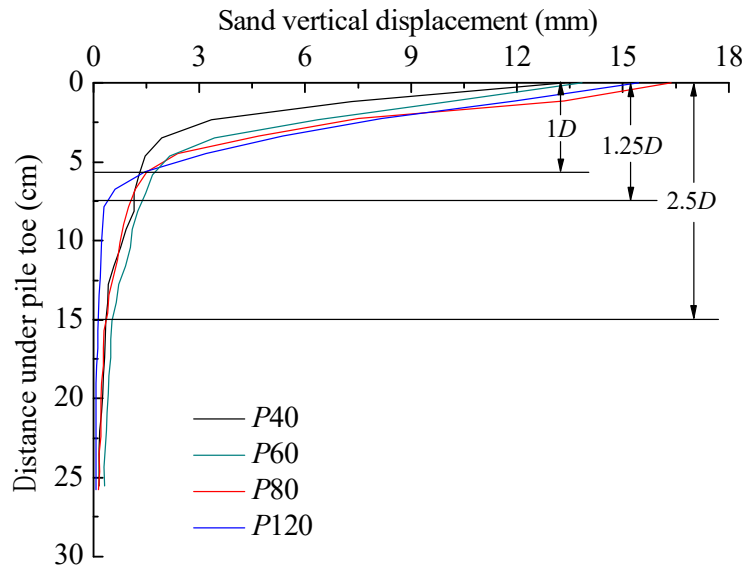
311 Figure 8 The sand displacement contours, drawn to the same scale, of the partially screw
 312 piles: (a) *P40*, (b) *P60*, (c) *P80*, and (d) *P120*, which were compressed to settlement $S=20$
 313 mm under the load tests.

314

315 2.6 Vertical displacement beneath the pile

316 The vertical displacement of sands beneath the pile is presented in Figure 9. The vertical
 317 displacement decreases nonlinearly with the depth. A significant displacement occurs to the

318 sands immediately beneath piles $P40$, $P60$ and $P80$, approximately in $1D$ range, and
 319 beneath pile $P120$, in the range of $1.25D$. Where the depth reaches $2.5D$, the vertical
 320 displacement reduces to a small constant value of about 0.1 to 0.5 mm depending on the
 321 piles of interest.

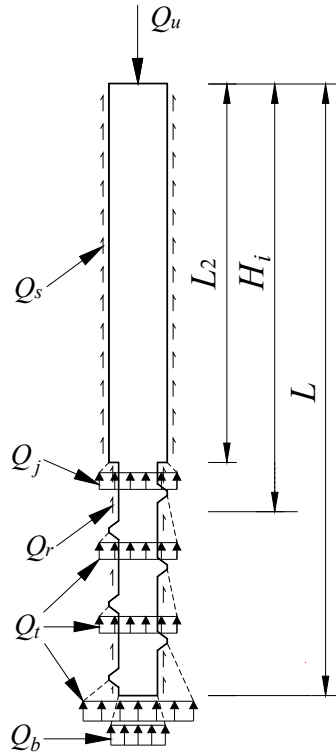


322
 323 Figure 9 The relationship of vertical displacement of sands beneath the piles and the depth.

324

325 2.7 Prediction of pile bearing capacity

326 The bearing capacity of the partially-screwed pile that is loaded vertically is contributed by
 327 five components of resistance, from the top to the bottom: the shaft skin friction, Q_s ,
 328 resistance of shaft–screw junction, Q_j , resistance of screw threads, Q_t , screw rod skin
 329 friction, Q_r , and the base resistance, Q_b . These components are presented diagrammatically
 330 in Figure 10. The corresponding values are determined in terms of the shear failure slips
 331 observed in the DIC imaging results and the corresponding methods.



332

333 Figure 10 Bearing capacity break-downs of partially-screwed pile under vertical loading.

334

335 The shaft skin friction Q_s and the screw rod skin friction Q_r arises from a cylindrical

336 shaft–sand failure (Figure 7), and as suggested by Nasr [30], are determined in terms of the

337 following expressions:

$$Q_s = 0.5\pi D \gamma' L_2^2 \beta \quad (2)$$

$$Q_r = 0.5\pi d \gamma' (L^2 - L_2^2) \beta \quad (3)$$

338 where γ' is the submerged unit weight of sand, $\beta = K \tan \delta'$, K is the coefficient of

339 lateral earth pressure, and δ' is the effective friction angle between the soil and pile

340 material. The factor K is dependent on the depth of the point of interest, nature of the pile

341 installation and soil conditions. According to [31-33], K varies between Rankine's active

342 and passive earth pressure coefficients, and in some cases exceeds Rankine's passive earth

343 pressure coefficient. Alawneh *et al.* [34] conducted a series of model tests on piles installed

344 in sandy soil. The soil properties, and other conditions including the pile diameter and shaft
 345 surface characteristics were consistent with those used in this study. In their tests, K ranged
 346 between 3.18 and 4.33. Based on the range, $K = 3.5$ was assumed in this study.

347

348 The failure slips of sands that are in the proximity of the shaft–screw junction and the screw
 349 threads (except the bottommost one) were constrained to limited zones (Figure 7),
 350 replicating a local failure pattern. The sands below the bottommost threads and the sands
 351 underneath the piles were concurrently failed along continuous slips, propagating
 352 downward spirally to relatively larger areas, as presented in the DIC imaging results (Figure
 353 7). This pattern replicates global, connected failure slips as occurred to a foundation soil
 354 which is vertically loaded as discussed by Terzaghi. In terms of the recorded failure patterns,
 355 the resistances at the shaft–screw junction, Q_j , the resistance as a sum of the threads, Q_t , and
 356 the base resistance, Q_b , as per [35], are expressed as:

$$Q_j = A_s (\gamma' L_2 N'_q + 0.5 \gamma' D N'_\gamma) \quad (4)$$

$$Q_t = A_s \left[\sum_{i=1}^{m-1} (\gamma' H_i N'_q + 0.5 \gamma' D N'_\gamma) + \gamma' H_m N_q + 0.5 \gamma' D N_\gamma \right] \quad (5)$$

$$Q_b = A_b (\gamma' L N_q + 0.5 \gamma' d N_\gamma) \quad (6)$$

357 where A_s is the projected area of threads and equals $\pi(D^2 - d^2)$, A_b is the area of pile base
 358 and equals πd^2 , m is the count of threads, H_i is the location of thread i , (N'_q, N'_γ) and $(N_q,$
 359 $N_\gamma)$ are Terzaghi's bearing capacity factors for local and general shear failures respectively,
 360 and as provided in [36] are determined as a function of soil shear strength.

361

362 The five components of resistance interact when the pile is compressed to attain its ultimate

363 bearing capacity. The interactions are dependent on the pile dimension ratio χ . In terms of
364 the test results obtained by Mohajerani *et al.* [10], a greater dimension ratio contributes to a
365 greater ultimate bearing capacity, and vice versa. Their study proposed to estimate the
366 ultimate bearing capacity of partially-screwed pile in sand using the following equation:

$$Q_u = \chi(Q_s + Q_j + Q_t + Q_r + Q_b) \quad (7)$$

367 The ultimate bearing capacities of piles that are predicted in terms of Eq. (7) are provided in
368 Table 2. In this table, the ultimate bearing capacities obtained from the tests are also
369 provided for comparison. We assessed the prediction accuracy by determining the ratio of
370 the predicted value to the test result of each pile. The ratios range from 76.3% to 95.4% for
371 the piles tested, suggesting varied levels of prediction. The best prediction applies to pile
372 P40, and the least to pile P120. It appears that the prediction accuracy is positively related
373 to the pile dimension ratio χ , at least for the piles examined in this study. There are at least
374 two reasons: i) the χ value was not accounted for when $S = 0.2D$ criterion was determined.
375 The Q_u is related to not only the settlement, but also the geometric characteristics of piles.
376 This is evidenced from the P - S curves where locations of greatest curvature and drastic
377 drop varied among the piles tested; and ii) a single multiplier of χ in Eq. (7) less likely
378 captures the interactions between the shaft, threads and sands, although it has added to the
379 prediction of Q_u . For instance, χ normalises the pile dimension and therefore likely neglects
380 effects of underlying factors (i.e., thread pitch and pile diameter). The size effects, however,
381 sometimes clearly influence the pile bearing capacity. This is evidenced from Eq. (7) of
382 consistently underestimating Q_u , as the piles used in the current study were downscaled and
383 less in dimension than those used in [10] which developed Eq. (7). We therefore suggest

384 additional research to be completed to improve the prediction of bearing capacity. This goal
 385 can be attained by conducting numerical simulations.

386 Table 2 Comparisons between the estimated ultimate bearing capacities and the test results.

Pile	Q_u , predicted result (kN)	Q_u , load test result (kN)	Rate of prediction
<i>P40</i>	1.097	1.150	95.4%
<i>P60</i>	1.123	1.301	86.3%
<i>P80</i>	1.059	1.301	81.4%
<i>P120</i>	0.726	0.952	76.3%

387

388 **3 DEM Simulations**

389 The DEM simulations were conducted to examine the shaft- and thread–sand interactions,
 390 to determine the components of resistance more accurately and therefore to improve the
 391 prediction of the ultimate bearing capacity. DEM simulations were conducted on the
 392 partially-screwed pile in the earlier study [5]. The DEM model in that study was developed
 393 to simulate load tests that are similar, in the set-up, piles, sands and test procedures, to those
 394 used in the present study. The only difference is the varied pitches of piles that were
 395 examined in the present study, whereas a single pitch was used in the early study. Therefore,
 396 we adapted the previous DEM model to suit the changes. The model was discussed in brief
 397 herein and the details were provided in [5].

398

399

400 **3.1 The DEM model**

401 An assembly of discs was poured under gravity into a two-dimensional container of 600 (W)
402 \times 1,100 (H) mm. The sizes agree with those of AOI that was used in the DIC analysis. The
403 diameters of discs ranged between 2.4 to 4.8 mm. The diameters were up-scaled to reduce
404 the disc number to a value at which the system can conduct stable computation and provide
405 reliable simulation results. As a result the number was effectively reduced from 840,000 to
406 50,618. This size upscaling method has been used in many previous DEM simulations on
407 various particles (e.g. [5, 37-39]) and were verified of its capability and effectiveness in
408 obtaining reliable simulation results. The diameter was determined through a parametric
409 study which examined choices of diameter and respective convergence with the test P - S
410 curves. Once the assembly settled and the contact force was damped to its normal range, a
411 fraction of particles was removed to create the space for the piles. This was attained by the
412 ray casting approach [5] whereby a set of closed form that replicates the outline of the pile
413 was created in the location that the pile should be erected. The enclosed discs were deleted
414 by the simulation program. An example of the resulted model is presented in Figure 11. As
415 in the load tests, all of the simulated piles were compressed down at a rate of 0.3 mm/min
416 and the resulted P - S curves were captured.

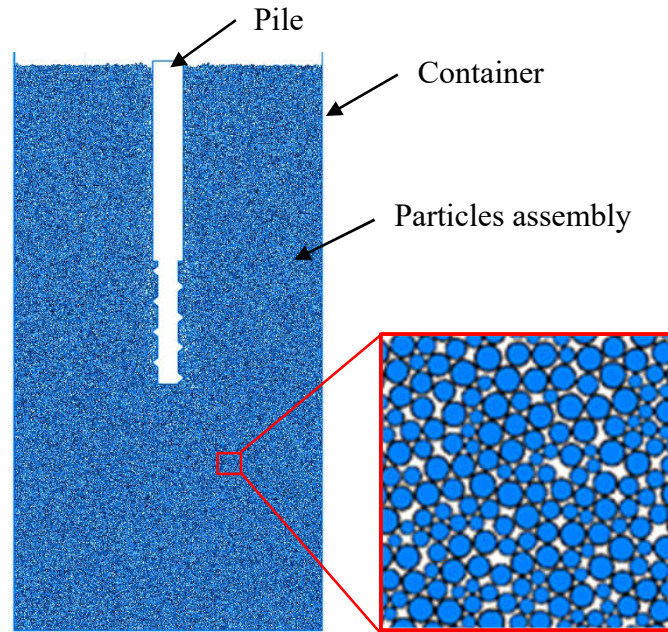


Figure 11 The DEM model of the partially-screwed pile.

417

418

419

420 As for the DEM simulation in [5], this present study used the linear contact model to
 421 simulate disc–disc and disc–wall interactions. The model parameters and corresponding
 422 values are provided in Table 3. These parameters were determined by harmonising the
 423 values so that the P – S curves from the simulations agreed with corresponding curves
 424 obtained in the load tests. As representative examples, P – S curves of piles $P60$ and $P120$
 425 are provided in Figure 12. Acceptable agreement between the simulation and test results
 426 was attained. There were less significant fluctuations present at some sections. As discussed
 427 in [5] and other DEM studies, the fluctuations are normal appearance of DEM simulation
 428 curves which mainly arise from the time-step dependent algorithms of DEM and the
 429 damping resulted delays. A convention is to focus on the trendlines which was adopted in
 430 this study.

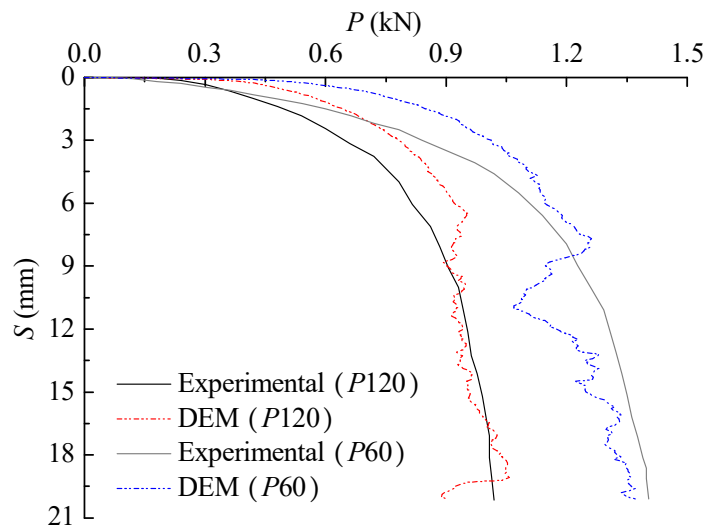
431

432

Table 3 Micromechanical properties for DEM simulation.

Parameter	Value
Particle	
Density	$2.65 \times 10^3 \text{ kg/m}^3$
Particle diameter	2.4–4.8 mm
Normal stiffness and shear stiffness	$1.9 \times 10^7 \text{ N/m}$
Friction coefficient	0.53
Local damping	0.7
Wall	
Normal stiffness and shear stiffness	$1.9 \times 10^7 \text{ N/m}$
Fiction coefficient	0.5

433



434

435 Figure 12 The $P-S$ curves of piles $P60$ and $P120$ obtained from the DEM simulations and
 436 laboratory tests.

437

438 Although DEM simulation takes advantages in addressing engineering problems in granular

439 and discontinuous materials, there have been limitations identified with its applications. The
440 first is the scale to model. DEM uses an assembly of up to millions of particle number to
441 simulate structures or soils and capture its dynamics. The simulation is relatively
442 computationally intensive, which limits either the length of a simulation or the number of
443 particles. This limitation becomes less significant due to advances in computing power,
444 numerical algorithms and parallel processing capabilities (shared or distributed systems),
445 however remains. The other limitation is determination of model parameters. Many
446 parameters involve micro-mechanical properties (e.g. particle stiffness) and are difficult to
447 measure directly or individually. Indirect calibration is widely accepted and applied, which
448 however is suboptimal due to concern of suitability to new materials. Similar suitability
449 concern arises from contact models adopted in DEM studies. The models are idealized into
450 a range of categories, e.g. linear elastic, nonlinear elasto-plastic, rolling resistance and
451 frictional models, however sometimes are chosen vaguely. DEM elements are also limited
452 in replicating particle shapes, although clumps and clusters are used to reflect
453 texture/angularity of particles. Nonetheless, this particle shape discrepancy is usually
454 accounted for by adjusting element micro-mechanical properties so that in-bulk mechanical
455 behaviour is captured. Conversely DEM provides a numerical tool of simulating discrete
456 matter of a relatively small-scale system, and of describing the micro-mechanical behaviour
457 of the system including particle contact force, grain crushing and particle breakage. To this
458 end, DEM simulations are suitable for granular materials and many geomaterials (e.g., coal,
459 ores, soil, rocks and aggregates) to examine the particulate-scale physical processes and
460 explain the phenomena that is otherwise impossible to observe and discuss using

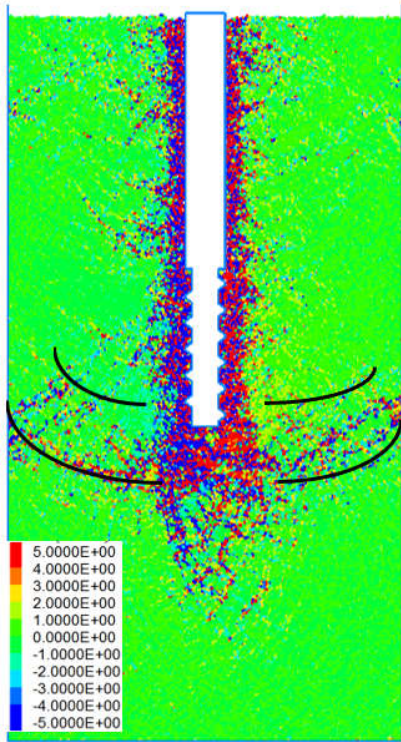
461 experiment. However, to model a real scale problem, numerical tools for continuum matter
462 is still preferable.

463

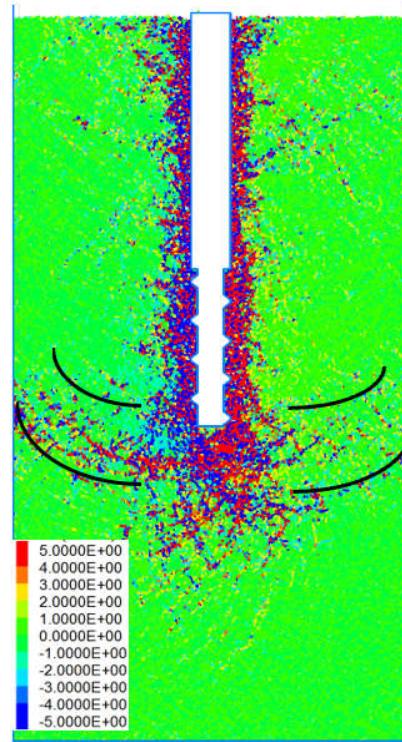
464 **3.2 Numerical results**

465 **3.2.1 Particle rotation field**

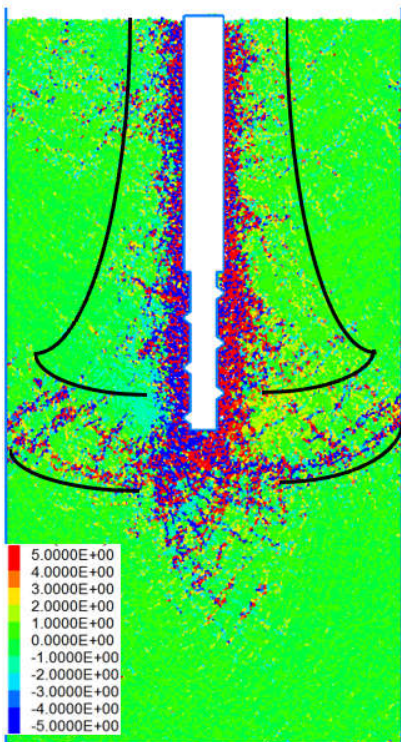
466 The particle rotation field is related to the formation and development of the soil sliding
467 surface. Usually, the particles rolling on the sliding surface is more obvious than that of the
468 other parts [37, 40]. The particle rotation fields surrounding the piles that are compressed to
469 the final state are provided in Figure 13. On these field maps, define clockwise rotations as
470 positive and mark any rotations greater than $+5^\circ$ (and -5°) to be $+5^\circ$ (and -5°). The rotations
471 of the particles near the screw section and the pile base are significant. For pile *P80*, the
472 lateral rotation influence zone is the largest and increases from pile top to base, and the load
473 is transferred to a wider range of particles. In contrast, piles *P40* and *P120* have less
474 noticeable rotation zones and present the cylindrical distribution. On pile *P120*, an
475 approximate symmetrical rotation band exists beneath the bottom thread. For all piles
476 except for pile *P120*, a continuous sliding surface is formed in the particles assembly and a
477 general shear failure mode evolves.



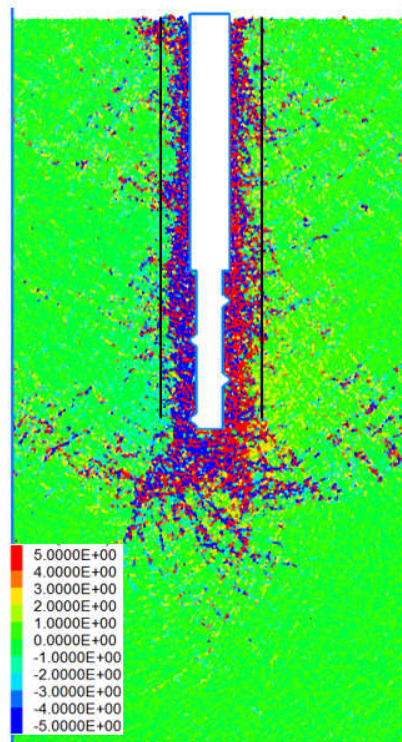
(a)



(b)



(c)



(d)

478 Figure 13 Particle rotation fields of the partially-screwed piles: (a) P40, (b) P60, (c) P80

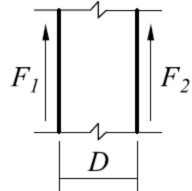
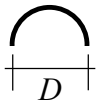
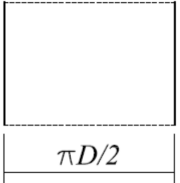
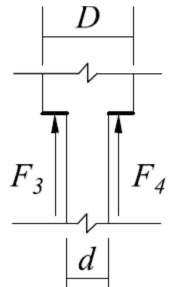
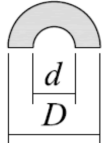
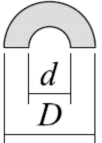
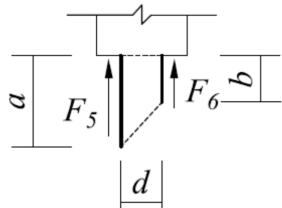

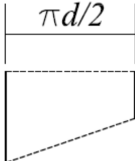
479 and (d) *P120*, which are compressed to settlement $S=20$ mm under the load tests.

480

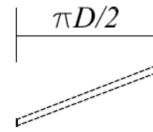
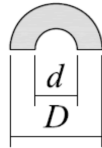
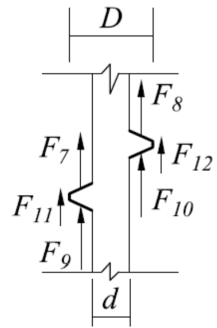
481 **3.2.2 Bearing capacity**

482 The DEM program can capture contact force at any locations, which sheds light on ultimate
483 bearing capacity. A barrier to tackle is to transform the contact forces captured in the
484 two-dimensional simulation to equivalent resistance in the three-dimensional space in which
485 the load tests were conducted. We used the approach developed in [5] to determine the
486 equivalent resistance. It requires integrating the contact force with respect to the
487 circumference of pile. Given the force being radially constant, we multiplied the contact
488 force by a half of circumference (due to the semicircle cross section of pile) and obtained
489 the equivalent resistance. As with the load tests, we divided the pile into the five
490 components, i.e., the shaft skin, shaft–screw junction, screw threads, rod skin and the base,
491 and determined the equivalent resistances. The diagrams and the corresponding bearing
492 capacities are provided in Table 4.

Table 4 Load resistance provided by the components of pile obtained from the DEM simulations.

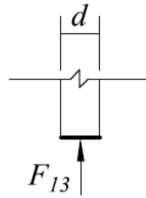
Component	Diagram			Load resistance
	Profile	Plan	Contact Surface	
Shaft skin				$Q_s = \frac{\pi D(F_1 + F_2)}{4} \quad (8)$
Shaft-screw junction				$Q_j = \frac{\pi(D+d)(F_3 + F_4)}{8} \quad (9)$
Rod skin				$Q_r = \frac{\pi d(a+b)\left(\frac{F_5}{a} + \frac{F_6}{b}\right)}{8} \quad (10)$

Screw thread, as
per [10, 41]



$$Q_t = \frac{\pi(D+d)(F_7 + F_8 + F_9 + F_{10})}{8} + \frac{\pi D(F_{11} + F_{12})}{4} \quad (11)$$

Base



$$Q_b = \frac{\pi d F_{13}}{8} \quad (12)$$

495 To meet the goal of optimising geometric characteristics of pile, it is worth examining the
 496 load contributions of individual sections of pile. The sections include the shaft, screw and
 497 the base. Their contributions to the bearing capacity, i.e., the load share ratio, are provided
 498 in Table 5. The results apply to the point of settlement $S = 20$ mm. Varied load share ratios
 499 are present across the piles tested. The greatest load share occurred to the screw sections,
 500 which shared 52.2% to 61.3% of the loads, depending on the choices of pile. The sands at
 501 the base supported about a quarter of the load. The rest load share of less than 20% on
 502 average was carried by the shaft skin. The load share percentage is different from that of a
 503 shaft pile that sits on sands which is usually classified an end-bearing pile. It is plausible to
 504 suggest that the presence of screw section has noticeably influenced the load share pattern,
 505 and thus the load transfer. The partially-screwed piles effectively enable the interaction with
 506 sands adjacent the screw section and prompt the skin friction. Greatest pile–sand
 507 interactions occurred to piles *P60* and *P80* which used dimension ratios $\chi = 1$ and 1.33
 508 respectively. The two factors coincide with the two optimal factors that were identified in
 509 the load tests. The coincidence verifies the presence of the optimal dimension ratios, and its
 510 influence. The influence can be understood by further breaking down the load shares of
 511 screw sections.

512 Table 5 Load sharing ratios of different sections of piles.

Pile	Load share of pile sections		
	Shaft section	Screw section	Pile base
<i>P40</i>	22.6%	52.2%	25.2%

<i>P60</i>	16.6%	61.3%	22.1%
<i>P80</i>	17.3%	58.9%	23.8%
<i>P120</i>	18.6%	55.6%	25.8%

513

514 The load share of the threads and rod skin, in relation to the load carried by the screw
515 sections, are provided in Table 6. The threads were counted from the bottom of each pile,
516 and numbed as from No. 1 to up to No. 6 depending on the thread counts. Between the
517 threads and rod skins, thread 1 shared the most of the load carried by the screw section, for
518 all of the piles tested. The shares ranged from 45.7% to 39.5%. The components that shared
519 the second most load were the rod skin for piles *P60*, *P80* and *P120*, and thread 4 for pile
520 *P40*. Each of the rest threads shared 0.3% to 21.6% of the loads. The significant variation in
521 load sharing suggests that some of the threads were not at its capacity of load sharing, or the
522 pitch was not chosen appropriately. An example is thread 6 of pile *P40* which contributed
523 marginally. As opposed to pile *P40*, pile *P120* distributed the loads in a better proportion to
524 its threads. This pile however did not provide the bearing capacity Q_u as much as the other
525 partially-screwed piles do (Figure 5). We sought to optimise the pitch considering the
526 bearing capacity and the well-apportioned load shares. To this end, pile *P80* was
527 recommended which offered the most Q_u , enabled threads most, and used less count of
528 threads. Its dimension ratio $\chi = 1.33$ can be used as a reference point in further studies.

529 Table 6 Load sharing ratios of threads and rod skin at the screw sections of piles.

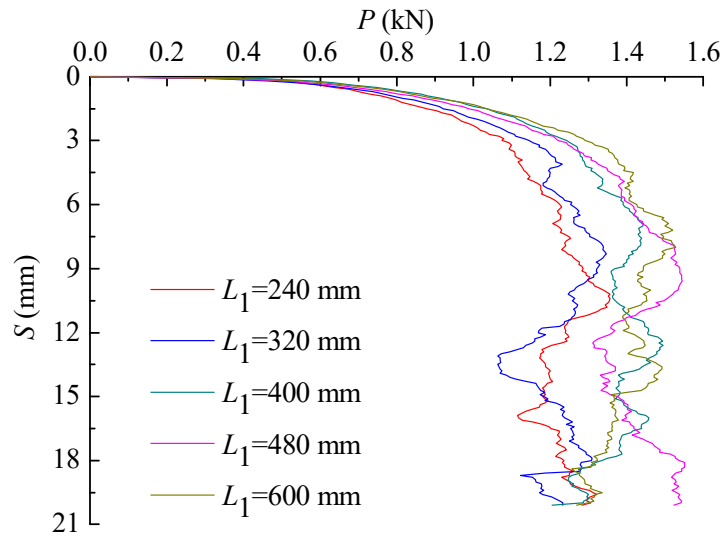
Pile	Load share of threads and rod skin						
	Thread 1	Thread 2	Thread 3	Thread 4	Thread 5	Thread 6	Rod skin

<i>P40</i>	39.5%	12.7%	7.8%	14.4%	13.2%	0.3%	12.1%
<i>P60</i>	45.2%	5.8%	10.8%	6.9%	–	–	31.3%
<i>P80</i>	45.7%	14.5%	9.4%	–	–	–	30.4%
<i>P120</i>	44.5%	21.6%	–	–	–	–	33.9%

530

531 In addition to the pitch, the proportion of screw section, L_1 , was varied, to examine its
532 effects on the pile bearing capacity. The additional choices of length that were considered
533 included $L_1 = 320, 400, 480$ and 600 mm. The scenario of $L_1 = 600$ mm represented a
534 fully-screwed pile. For these scenarios, the remaining geometric characteristics of piles
535 were kept unchanged. They included the outside diameter $D = 60$ mm and thread pitch $H =$
536 80 mm. The DEM model was applied to these scenarios and the P – S curves of these
537 scenarios are provided in Figure 14. All of the curves develop similarly linearly where the
538 settlement $S < 1$ mm. The similarity suggests that the length of the screw section has
539 marginal effect on the early-stage bearing capacity. Where $S > 1$ mm, the P – S curves differ
540 in shape and the bearing capacity increases in various rates. In terms of the $S = 0.2D$ failure
541 criterion, the ultimate bearing capacity Q_u is 1.240 kN for the pile of $L_1 = 240$ mm, 1.169
542 kN for $L_1 = 320$ mm, 1.454 kN for $L_1 = 400$ mm, 1.363 kN for $L_1 = 480$ mm, and 1.407 kN
543 for $L_1 = 600$ mm, respectively. Where L_1 is between 240 to 400 mm, Q_u increases clearly
544 with L_1 , at a rate of 24.4% . Where $L_1 > 400$ mm, the increase rate drops to 3.2% to 6.3% .
545 The fully-screwed pile builds upon Q_u , but at the cost of shaft section of counteracting the
546 axial force, provided the pile length is fixed. Given the trade-offs between the shaft section

547 and the screw section, it is suggested that the length of screw section is generally not more
548 than 2/3 of length of piles that are installed in sands.

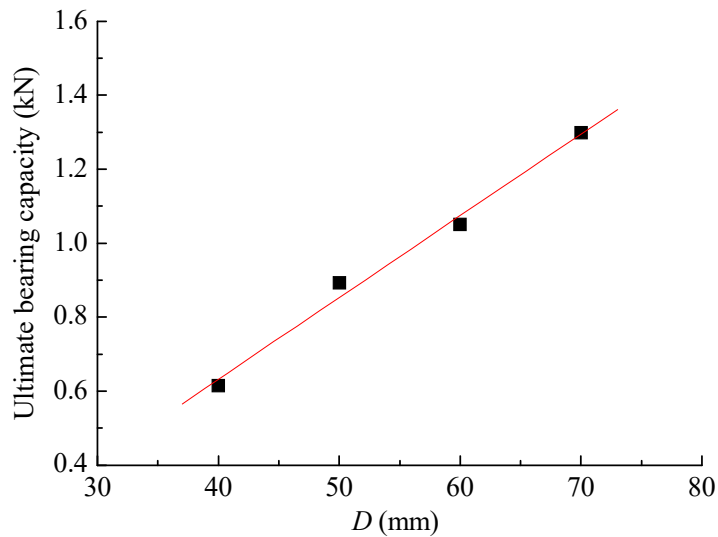


549

550 Figure 14 The P - S curves of piles with different length of screw section L_1 .

551

552 The other geometric characteristic of pile that we examined was the shaft diameter D . The
553 choices that we considered included $D = 40, 50, 60$ and 70 mm. We fixed the remaining
554 geometric characteristics: the dimension ratio $H/D = 1.0$, the length of screw section $L_1 =$
555 240 mm. Similarly, the DEM model was applied to these scenarios and the obtained P - S
556 curves were assessed in terms of the $0.2D$ failure criterion. The ultimate bearing capacity
557 was determined as 0.614 kN for the pile with $D = 40$ mm, 0.892 kN for $D = 50$ mm, 1.175
558 kN for $D = 60$ mm, and 1.298 kN for $D = 70$ mm. The results are provided in Figure 15. A
559 linear relationship exists between the ultimate bearing capacity and the shaft diameter,
560 where the diameter ranges between 40 to 70 mm. Therefore, improving the shaft diameter
561 effectively builds to the ultimate bearing capacity of the partially-screwed pile which agrees
562 with the expectation.



563

564 Figure 15 Relationship between the ultimate bearing capacity Q_u and pile shaft diameter

565 D .

566

567 4 Conclusions

568 This study examined effects of geometric characteristics of partially-screwed pile on the

569 pile performance. The examination was completed through the laboratory model tests,

570 digital image correlations and discrete element modelling simulations. The performance that

571 was examined included the P - S curves, ultimate bearing capacity, pile-sand interactions,

572 sand displacement vectors, and load shares of pile sections. The research work arrived at the

573 following conclusions.

574 (1) The ultimate bearing capacity reached the maximum value where the dimension

575 ratio of pitch to pile diameter ranged from 1.0 to 1.33. Piles that were in this

576 suggested range can effectively influence sands adjacent to the screw threads and

577 optimally enable the sands to share the load acted on the pile. The ultimate bearing

578 capacity increased nonlinearly with the presence of the screw section. Apportioning

579 2/3 of the pile length to the screw section was suggested to optimise the bearing
580 capacity and axial force resistance of pile.

581 (2) The screw section shared the load in a capacity greater than the shaft section of the
582 same pile does, for the scenarios examined in this study. Meanwhile, the screw
583 section contributed to the bearing capacity much greater than the corresponding
584 section of shaft pile. The bottommost thread provided the highest resistance, as
585 opposed to the remaining threads. The sands next to the shaft section and screw rod
586 failed due to skin friction; the sands surrounding the upper threads failed in local
587 shear slips; and at the bottommost thread and pile base, sands failed in globally
588 connected slips.

589 (3) An equation that predicts the ultimate bearing capacity of partially-screwed pile was
590 developed in terms of [Mohajerani *et al.* [10]]. The rate of prediction however
591 decreased with the thread pitch. The pitch count and pile dimension ratio were
592 suggested to be accounted for to improve the prediction.

593

594 **Acknowledgements**

595 This research is supported by the National Natural Science Foundation of China (No.
596 51408254, 51708245) and the Six Talent Peak Projects of Jiangsu Province (No. JZ-051).

597

598 **References**

599 [1] Livneh B, El Naggar MH. Axial testing and numerical modeling of square shaft helical
600 plies under compressive and tensile loading. Canadian Geotechnical Journal.

601 2008;45(8):1142-55.

602 [2] Tsuha CDC, Aoki N. Relationship between installation torque and uplift capacity of
603 deep helical piles in sand. *Canadian Geotechnical Journal*. 2010;47(6):635-47.

604 [3] Meng Z, Chen JJ, Zhang LY, Wang JH, Yao JM. Field tests to investigate the installation
605 effects of drilled displacement piles with screw-shaped shaft in clay. *Journal of*
606 *Geotechnical and Geoenvironmental Engineering*. 2015;141(12):06015010.

607 [4] Zarrabi M, Eslami A. Behavior of piles under different installation effects by physical
608 modeling. *Int J Geomech*. 2016;16(5):04016014.

609 [5] Chen Y, Deng A, Wang A, Sun H. Performance of screw–shaft pile in sand: Model test
610 and DEM simulation. *Computers and Geotechnics*. 2018;104(118-30).

611 [6] Zuo H, Jin N, Xu C. Experiment on vertical bearing capacity of screw grout pile in
612 cohesive area. *Shenyang Jianzhu Daxue Xuebao (Ziran Kexue Ban)/Journal of Shenyang*
613 *Jianzhu University (Natural Science)*. 2016;32(2):225-31.

614 [7] Adams JI, Klym TW. A study of anchorages for transmission tower foundations.
615 *Canadian Geotechnical Journal*. 1972;9(1):89-104.

616 [8] Rao SN, Prasad Y, Veeresh C. Behaviour of embedded model screw anchors in soft clays.
617 *Geotechnique*. 1993;43(4):605-14.

618 [9] Bagheri F, El Naggar MH. Effects of installation disturbance on behavior of multi-helix
619 piles in structured clays. *DFI Journal - The Journal of the Deep Foundations Institute*.
620 2016;9(2):80-91.

621 [10] Mohajerani A, Bosnjak D, Bromwich D. Analysis and design methods of screw piles: A

622 review. *Soils and Foundations*. 2016;56(1):115-28.

623 [11] Sakr M. Installation and performance characteristics of high capacity helical piles in
624 cohesionless soils. *DFI Journal - The Journal of the Deep Foundations Institute*.
625 2011;5(1):39-57.

626 [12] Fahmy A, El Naggar MH. Cyclic axial performance of helical-tapered piles in sand.
627 *Geotechnical and Geological Engineering*. 2016;10(3):98-110.

628 [13] Choi Y, Kim DC, Kim SS, Nam MS, Kim TH. Implementation of noise-free and
629 vibration-free PHC screw piles on the basis of full-scale tests. *Journal of Construction*
630 *Engineering and Management*. 2013;139(8):960-7.

631 [14] Sakr M. Performance of helical piles in oil sand. *Canadian Geotechnical Journal*.
632 2009;46(9):1046-61.

633 [15] Li W, Deng L. Axial load tests and numerical modeling of single-helix piles in
634 cohesive and cohesionless soils. *Acta Geotechnica* 2019;14(461-75

635 [16] Meng Z, Chen JJ, Wang JH. Numerical analysis of bearing capacity of drilled
636 displacement piles with a screw-shaped shaft in sand. *Mar Georesour Geotec*.
637 2017;35(5):661-9.

638 [17] Qian J, Wang B, Chen H, Huang M. Model test and bearing mechanism study on
639 grouting-screw uplift pile. *Journal of Building Structures*. 2015;36(10):146-52.

640 [18] George BE, Banerjee S, Gandhi SR. Numerical analysis of helical piles in cohesionless
641 soil. *International Journal of Geotechnical Engineering*. 2017:1-15.

642 [19] Lee CW, Kim YS, Park SY. Development of prebored screw pile method and
643 evaluation of its bearing characteristics. *Mar Georesour Geotec*. 2016;34(1):42-56.

- 644 [20] Xu PH, Xu B, Dong TW. The analysis of the bearing capacity of screw piles on static
645 loading test. *Journal of Transport Science and Engineering*. 2016;32(3):58-62.
- 646 [21] Aoyama S, Mao WW, Goto S, Towhata I. Application of advanced procedures to model
647 tests on the subsoil behavior under vertical loading of group pile in sand. *Indian*
648 *Geotechnical Journal*. 2016;46(1):64-76.
- 649 [22] Rao S, Nasr A. Behavior of vertical piles embedded in reinforced sand under pullout
650 oblique loads. *International Journal of Geotechnical Engineering*. 2010;4(2):217-30.
- 651 [23] Chen Y, Wang X, She Y, Cai J, Chen S. Macroscopic and mesoscopic working
652 performance of pcc pile subjected to vertical load. *Yanshilixue Yu Gongcheng*
653 *Xuebao/Chinese Journal of Rock Mechanics and Engineering*. 2015;34(7):1503-10.
- 654 [24] Nasr AMA. Uplift behavior of vertical piles embedded in oil-contaminated sand.
655 *Journal of Geotechnical & Geoenvironmental Engineering*. 2012;139(1):162-74.
- 656 [25] Sutton MA, Yan JH, Tiwari V, Schreier HW, Orteu JJ. The effect of out-of-plane
657 motion on 2D and 3D digital image correlation measurements. *Optics and Lasers in*
658 *Engineering*. 2008;46(10):746-57.
- 659 [26] Hall SA, Bornert M, Desrues J, Pannier Y, Lenoir N, Viggiani G, et al. Discrete and
660 continuum analysis of localised deformation in sand using X-ray mu CT and volumetric
661 digital image correlation. *Geotechnique*. 2010;60(5):315-22.
- 662 [27] Pan B, Asundi A, Xie HM, Gao JX. Digital image correlation using iterative least
663 squares and pointwise least squares for displacement field and strain field measurements.
664 *Optics and Lasers in Engineering*. 2009;47(7-8):865-74.

- 665 [28] Knappett JA, Haigh SK, Madabhushi SPG. Mechanisms of failure for shallow
666 foundations under earthquake loading. *Soil Dynamics and Earthquake Engineering*.
667 2006;26(2-4):91-102.
- 668 [29] Tsuha CDHC, Thorel L, Rault G, Garnier J. Evaluation of the effect of installation on
669 the helical pile performance in sand by centrifuge tests. 1st International Geotechnical
670 Symposium on Helical Foundations. France: ISHF, 2013. p. 311-22.
- 671 [30] Nasr M. Performance-based design for helical piles. *Contemporary Topics in Deep*
672 *Foundations*. USA: American Society of Civil Engineers, 2009. p. 496–503.
- 673 [31] Nasr AMA. Uplift behavior of vertical piles embedded in oil-contaminated sand.
674 *Journal of Geotechnical and Geoenvironmental Engineering*. 2013;139(1):162-74.
- 675 [32] Miller GA, Lutenecker AJ. Influence of pile plugging on skin friction in
676 overconsolidated clay. *Journal of Geotechnical & Geoenvironmental Engineering*.
677 1997;123(6):525-33.
- 678 [33] Liu F, Jiang MJ, Zhu FY. Discrete element analysis of uplift and lateral capacity of a
679 single pile in methane hydrate bearing sediments. *Computers and Geotechnics*.
680 2014;62(61-76).
- 681 [34] Alawneh AS, Malkawi AIH, Aldeeky H. Tension tests on smooth and rough model
682 piles in dry sand. *Canadian Geotechnical Journal*. 1999;36(4):746-53.
- 683 [35] Society CG. *Canadian Foundation Engineering Manual*, 4th Ed. 4th Ed ed. Vancouver,
684 B. C., Canada: Canadian Geotechnical Society, 2006.
- 685 [36] Murthy VNS. *Geotechnical Engineering: Principles and Practices of Soil Mechanics*
686 *and Foundation Engineering*. New York: Marcel Dekker Inc, 2003.

- 687 [37] Jiang MJ, Xiao Y, Chen SL, Hu HJ, Wu XF. Discrete element analysis of bearing
688 mechanism of single pile in sand under vertical load. *Yantu Lixue/Rock and Soil Mechanics*.
689 2010;31(SUPPL. 2):366-72.
- 690 [38] Wang C, Deng A, Taheri A. Three-dimensional discrete element modeling of direct
691 shear test for granular rubber–sand. *Computers and Geotechnics*. 2018;97(204-16).
- 692 [39] Liu Y, Deng A, Mark J. Three-dimensional modeling of geocell-reinforced straight and
693 curved ballast embankments. *Computers and Geotechnics*. 2018;102(53-65).
- 694 [40] Tang HX, Dong YF, Chu XH, Zhang X. The influence of particle rolling and
695 imperfections on the formation of shear bands in granular material. *Granular Matter*.
696 2016;18(1):1-12.
- 697 [41] Elsherbiny. ZH, El Naggar MH. Axial compressive capacity of helical piles from field
698 tests and numerical study. *Canadian Geotechnical Journal*. 2013;50(12):1191-203.
- 699